Talanta 281 (2025) 126760

Contents lists available at ScienceDirect

Talanta

journal homepage: www.elsevier.com/locate/talanta

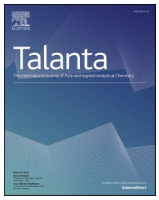

Plasmon-enhanced fluorescence and electrochemical aptasensor for SARS-CoV-2 Spike protein detection

Ruifeng Zhu [a,b], Mateo Alejandro Martínez-Roque [a], Gabriela Figueroa-Miranda [a], Ziheng Hu [a], Adriano Acunzo [a,c], Hangyu Li [a], Qinyu Hu [a], Justus Bednar [a,d], Thomas Gensch [e], Sven Ingebrandt [b], Andreas Offenhäusser [a], Dirk Mayer [a,*]

[a] Institute of Biological Information Processing, Bioelectronics (IBI-3), Forschungszentrum Jülich GmbH, 52428, Jülich, Germany
[b] Institute of Materials in Electrical Engineering 1, RWTH Aachen University, 52074, Aachen, Germany
[c] Department of Physics, University of Naples "Federico II", Via Cintia 26, Naples, 80126, Italy
[d] Fakultät für Mathematik, Informatik und Naturwissenschaften, RWTH Aachen University, 52074, Aachen, Germany
[e] Institute of Biological Information Processing, Molecular and Cellular Physiology (IBI-1), Forschungszentrum Jülich GmbH, 52428, Jülich, Germany

ARTICLE INFO

Keywords:
Gold nanopit arrays
Nanoimprint lithography
Plasmon-enhanced fluorescence
Electrochemical aptasensor
SARS-CoV-2 Spike protein

ABSTRACT

In this work, we combined plasmon-enhanced fluorescence and electrochemical (PEF-EC) transduction mechanisms to realize a highly sensitive dual-transducer aptasensor. To implement two traducers in one biosensor, a novel large-scale nanoimprint lithography process was introduced to fabricate gold nanopit arrays (AuNpA) with unique fringe structures. Light transmitting through the AuNpA samples exhibited a surface plasmon polariton peak overlapping with the excitation peak of the C7 aptamer-associated fluorophore methylene blue (MB). We observed a five and seven-times higher average fluorescence intensity over the AuNpA and fringe structure, respectively, in comparison to a plane Au film. Furthermore, the MB fluorophore was simultaneously utilized as a redox probe for electrochemical investigations and is described here as a dual transduction label for the first time. The novel dual transducer system was deployed for the detection of SARS-CoV-2 Spike protein via a C7 aptamer in combination with a strand displacement protocol. The PEF transducer exhibited a detection range from 1 fg/mL to 10 ng/mL with a detection limit of 0.07 fg/mL, while the EC traducer showed an extended dynamic range from 1 fg/mL to 100 ng/mL with a detection limit of 0.15 fg/mL. This work provides insights into an easy-to-perform, large-scale fabrication process for nanostructures enabling plasmon-enhanced fluorescence, and the development of an advanced but universal aptasensor platform.

1. Introduction

COVID-19 is an acute respiratory disease caused by the highly transmissible SARS-CoV-2 virus, a positive-sense single-segmented RNA virus with a genome size of approximately 30 Kb, infected individuals may exhibit symptoms like cough, fever, pneumonia, and complications, with potentially fatal outcomes [1]. Some of the now commonly used testing assays include computed tomography (CT) imaging, nucleic acid tests, gene sequencing, lateral flow assays, and serological assays, while the primary diagnostic method of COVID-19 is called reverse transcription-polymerase chain reaction (RT-PCR) test [1–4] which targets the viral genome in the nasal and nasopharyngeal samples. The RT-PCR is considered the gold standard and is generally designed to amplify one or more SARS-CoV-2 genes. Nonetheless, these technologies have some drawbacks, RT-PCR, for example, requires purified RNA, sophisticated equipment, and expensive probes [5].

Given the mentioned constraints of the conventional approaches, a rapid, cheap, and easily available system is needed to determine the presence of the infection during the incubation period to provide enough time for adapting the desirable treatment process and curb its high spread rate. Biosensor technology can be precisely designed for spotting SARS-CoV-2 by employing specific biorecognition elements like antibodies, antigens, proteins, whole viruses, nucleic acids, and aptamers [3]. Among them, aptamers have emerged as promising alternatives to antibodies in biosensing and diagnostics, which are synthetic, single-stranded oligonucleotides that bind to a specific target molecule with high affinity and specificity. In addition, they possess high robustness over temperature changes and chemical treatments,

* Corresponding author.
E-mail address: dirk.mayer@fz-juelich.de (D. Mayer).

https://doi.org/10.1016/j.talanta.2024.126760
Received 12 May 2024; Received in revised form 20 August 2024; Accepted 22 August 2024
Available online 26 August 2024

versatility regarding applications, and reproducibility in synthesis [6]. The SARS-CoV-2 Spike protein (S protein) has been established as a key target in the rapid diagnosis of COVID-19 and the development of innovative tests for detecting viral antigens [7]. This protein comprises two critical domains: the receptor-binding domain (RBD), responsible for binding to the human angiotensin-converting enzyme 2 (ACE2) receptor and facilitating the virus's entry into host cells, and the fusion domain, which mediates the fusion of host cell and viral membranes through the C-terminal S2 subunit [8].

Many different types of transducers can be utilized for the implementation of the biosensor, including optical, electrical, mechanical transducers, etc. There are advantages to each of these interrogation schemes, for instance, when optical transducers are employed, the biosensing procedure can be often monitored in real time, and while electrochemical procedures are applied, high sensitivity can be expected. More advanced, multi-transducer sensing concepts can be used allowing the cross-verification of the readouts, minimizing the risk of false-positive results, enhancing the detection range, or delivering more comprehensive information about the analyzed biological target [9,10]. Many research works on multi-transducer systems focus on the combination of surface plasmon resonance (SPR) and electrochemical (EC) techniques named SPR-EC [11]. The SPR empowers the monitoring of changes in optical properties in the proximity of the gold surface, while the same gold surface is used to record electrochemical processes within the Helmholtz layer of the same gold sample [12]. The Kretschmann-SPR configuration is known for its high refractive index sensitivity via plasmonic wavelength shift [13,14]. However, its bulky, prism-based optics make it challenging to merge with point-of-care (POC) electrochemical systems. In contrast, gold nanostructure-decorated substrates that facilitate extraordinary optical transmission (EOT) are more suitable for POC setups due to easier alignment and miniaturization, despite lower sensitivity [15,16]. One strategy to harness nanostructure-decorated substrates is to take advantage of the strong electric fields generated during surface plasmon polariton (SPP) excitation to enhance fluorescence, thereby improving plasmon-enhanced fluorescence (PEF) detection.

In this study, we introduce for the first time a novel approach of combining plasmon-enhanced fluorescence and electrochemical detection (PEF-EC) to monitor the binding events between the S protein of SARS-CoV-2 and the C7 aptamer receptor. This process is based on an EOT configuration using gold nanopit arrays (AuNpA), where plasmonic properties were exploited to enhance the fluorescence signal of methylene blue (MB), which was attached to the C7 aptamer. MB is a well-established redox reporter frequently utilized in electrochemical aptasensors [17]. Additionally, MB emits fluorescence light in the near-infrared region after excitation with a wavelength of 668 nm [18]. Thus, MB can be utilized as both electrochemical and fluorescence probe. However, only a few studies have explored these capabilities simultaneously. Chang et al. [19] reported the synthesis of an MB-encapsulated zeolitic imidazolate framework-90 (MB@ZIF-90) as a dual-signal biosensor for adenosine triphosphate (ATP) detection, utilizing fluorescence and electrochemical techniques. However, their detection system did not involve PEF but relied on processes occurring in bulk solution and a release of MB from MB@ZIF-90. In our experiment, PEF was used in combination with electrochemical measurements to implement a dual transducer aptasensor, which used the same probe for both transduction principles. The MB was tagged to the C7 S protein aptamer (referred to as S2_20T_MB) which was tethered to the gold surface decorated with nanopit arrays. These AuNpA were designed such that the SPP peak overlapped with the excitation wavelength of the MB to enable strong coupling effects. In addition, AuNpA exhibited fringe structures created through direct nanoimprint lithography (NIL) processes. Noteworthy, such additional nanostructures can lead to even stronger PEF processes. Besides the characterization of the fluorescence of our aptasensor, we investigated its voltammetric redox properties. To enable unambiguous sensor responses, we immobilized the aptamer to the gold surface via thiolated, partially complementary single-stranded DNA (ssDNA) molecules (S1). S1 could form a stem-loop structure following the dissociation of the S2_20T_ MB aptamer due to S protein binding and its release from the AuNpA surface. The monitoring of surface-associated binding processes by two independent transducer systems may enhance the sensor performance and can provide a better understanding of physicochemical processes at the solid-liquid interface.

2. Experimental section

Details on reagents and chemicals, Au nanopit arrays fabrication, gel electrophoresis experiment, NUPACK simulation, aptamer design, Finite-Difference Time-Domain (FDTD) simulation for ideal and AFM models, Fluorescence Lifetime Imaging (FLIM) characterization, Quartz Crystal Microbalance (QCM) characterization, and Surface Plasmon Resonance Microscopy (SPR-M) characterization are provided in the Supporting Information.

2.1. Electrochemical and fluorescent measurements

The PEF-EC dual signal measurement setup is illustrated in Fig. S2. Fluorescence microscopy images were captured using a ZEISS Axio Imager Z1 equipped (Zeiss, Jena, Germany) with the following components: a light source illuminator HXP120, a 63 × water immersion objective (Plan-Achroplan, NA 1.0), Zeiss 50 filter sets (Excitation 640/30 nm, beamsplitter: 660 nm, emission: 690/50 nm), an analy differential interference contrast (DIC) translight, and a digital CCD camera (model AxioCam MR R3). The scaled image size is 142.10 μm × 106.48 μm, featuring a 16-bit dynamic range and a scaling of 0.102 μm × 0.102 μm per pixel. 500 ms exposure time was used for each fluorescence image. Since the aptamer-target binding events occur homogeneously across the entire AuNpA, we measured the arithmetic mean fluorescence intensity of the whole image as a signal using ZEN Blue Edition 2012 software.

A portable EmStat potentiostat (PalmSens BV, GA Houten, The Netherlands) was connected to a PC via PSTrace 5.9 software for electrochemical data recording and processing. The reaction chamber was 3D printed using clear resin as the printing material. The central area of the chamber was half-open, allowing the AuNpA to be easily mounted and exposed to the microscopy objective lens in the vicinity. The non-exposed area was connected to EmStat potentiostat as the working electrode. The solution was introduced into the reaction chamber via a pipette and then rinsed using a peristaltic pump. Two Pt wires were fixed on the left and right central area of the chamber, respectively, and connected to the EmStat potentiostat as pseudo-reference and counter electrodes. The limited space in our portable electrochemical system made the use of a small but less stable Pt pseudo reference electrode necessary [20]. Square wave voltammetry (SWV) measurements were performed in Tris buffer (10 mM Tris, 150 mM NaCl, 5 mM KCl, pH 7.4) for electrochemical characterization of the sensor performance. SWV scans were swept between −0.6 and −0.2 V with an equilibration time of 5 s, potential steps of 0.005 V, amplitude of 0.02 V, and a frequency of 5 Hz.

2.2. Aptasensor preparation

Before incubation, the AuNpA was firstly cleaned by oxygen plasma (Diener electronic GmbH, Ebhausen, Germany) at 0.5 mPa for 3 min to remove any residues on the Au surface. Then the AuNpA was immersed in ethanol for 5 min to reduce the generated gold oxides and afterwards rinsed with Milli-Q water. The S1 solution was pretreated by incubating 10 mM TCEP (tris(2-carboxyethyl)phosphine) for 1 h to cleave the disulfide bond of the aptamer receptors in a high-salt Tris buffer (NaCl 1.0 M, $MgCl_2$ 1 mM, Tris 10 mM, pH 7.4). The nanostructured samples were incubated with the above solution for 16 h at room temperature to

immobilize the molecules on the surface through thiol-gold bonds. Then, the samples were thoroughly rinsed with the Tris buffer (NaCl 0.15 M, KCl 5 mM, Tris 10 mM, pH 7.4) to remove the non-bonded aptamer. Subsequently, the as-prepared samples were incubated with 0.5 mM 6-MCH (6-mercapto-1-hexanol) ethanol solution for 0.5 h to obtain a compact, self-assembled receptor layer by blocking the unmodified sites and suppressing unspecific binding. The excess 6-MCH molecules were removed by rinsing the AuNpA separately with ethanol for 3 times and consecutively with 10 mM Tris buffer for another 3 times. Lastly, S2 strands were incubated on the surface for 2 h at room temperature to hybridize with the S1 strand. The various C7 aptamer strands used in our experiments were purchased from Sangon Biotech including all modifications with covalently attached thiol linker and MB-redox tags, see the Supporting Information. For the S protein assay, the aptasensor was incubated in various concentrations of the analyte molecules for 30 min. After incubation, the nanostructured Au samples were rinsed with the Tris buffer to remove excess S protein molecules that were not specifically adsorbed.

3. Results and discussion

3.1. Unexpected fringe structures

To solve the discrepancy in the momenta of incident photons in free space and SPP at identical frequencies, several momentum-compensation coupling mechanisms have been devised, including prism and grating coupling, with the purpose of augmenting the wave vector of incident light within the dielectric medium. This augmentation is essential to establish the requisite matching conditions for exciting SPP. However, the utilization of a prism coupler for SPP excitation poses challenges in the context of on-chip integration, despite its remarkable performance. Consequently, employing diffraction to couple light to SPP modes through a diffraction grating represents a more favorable choice for integration with the PEF effect. In this scenario, incident light is diffracted into a series of beams described by $k_d = k_x + mG$, where k_d signifies the propagation constant of the diffracted light, k_x denotes the propagation constant of the incident light ($k_x = k_0 n_d \sin\theta$), G represents the wavenumber associated with the grating ($G = 2\pi/\Lambda$), with m taking on values of 0, ±1, ±2, and so forth, corresponding to the diffraction orders and the period length of the grating (Λ). Additionally, n_d characterizes the refractive index of the dielectric medium. The wavevector matching condition in this case becomes [21,22].

$$k_0 n_d \sin\theta + \frac{2\pi}{\Lambda} m = k_0 \sqrt{\frac{\varepsilon_m \varepsilon_d}{\varepsilon_m + \varepsilon_d}} \tag{1}$$

where ε_m and ε_d are the dielectric constants of the metal and dielectric layer.

In electrochemical sensing, a connected gold surface with a high electrochemical surface area is important for the immobilization of a large number of receptor molecules and to achieve a low limit of detection. Herein, the 3D AuNpA was chosen as substrate for both the PEF and the EC transducer. We aimed to streamline the fabrication process of AuNpA by employing a direct NIL process on resist (Fig. 1), as an alternative to the time-consuming fabrication involving a Cr-based hard mask from our previous work [16]. The resulting nanoimprinted AuNpA sample exhibited a hexagonally closed-packed (hcp) pit structure with an average diameter of 177 nm and a lattice constant of 501 nm in SEM images at 100 k magnification (Fig. 2a). While at 5 k magnification, the fringe structures were clearly present with anisotropic directionality, superimposed on the pit array on a larger scale (Fig. 2b). To gain deeper insights into the morphology and characteristics of these fringe structures, we utilized atomic force microscopy (AFM) and focused ion beam (FIB) sectioning (Fig. 2f and c). The AFM analysis indicated that the height of the fringe structures was approximately 80 nm, while the pits possessed a depth of around 50 nm. The cross-sectional views of the FIB images disclosed that the fringed structure was correlated with variations in the thickness of the mr-NIL200 resist. Differential interference contrast (DIC) microscopy images confirmed the presence of the fringe structures (Fig. 2d), while the DIC surface image of samples [16] with pit arrays at a lattice constant of 600 nm fabricated by using Cr as a hard mask was uniform (Fig. S3). Interestingly, even the unpatterned regions of the AuNpA samples exhibited irregular surface corrugations in AFM and SEM investigations (Fig. 2g and e).

In order to elucidate the underlying causes of these fringe structures, we conducted a comparative analysis involving an Au film deposited on the same sample stack (Quartz/mr-NIL200/Ti/Au) but without undergoing the NIL process. As illustrated in Fig. 2h, the imprint-free resist/Au film exhibited a noticeably smoother topography than the imprinted sample (Fig. 2e). Further investigations were performed including the SEM of the master mold (Fig. S4) and AFM of the Ormostamp mold, Fig. S5. These experiments showed that the master mold surface was smooth and homogeneous, while the Ormostamp mold, which was used for the actual imprint, showed some irregular structure presumably contributing to the formation of the fringes. These observations suggest that the recurring fringe structures are a result of the NIL process. We suspect that the additional fringe structure originates from inherent material properties of the resist in combination with the imprint process, due to the anisotropy and boundary conditions of the pattern. However, further investigations are needed to comprehensively understand the mechanisms at play and to devise strategies to mitigate or harness these fringe structures for potential applications.

3.2. Feasibility analysis of the PEF effect

Another critical aspect of establishing strong PEF effects is the distance between the fluorophore and the metal surface. It is perceived that PEF occurs when fluorophores are excited near the metal surface, typi-

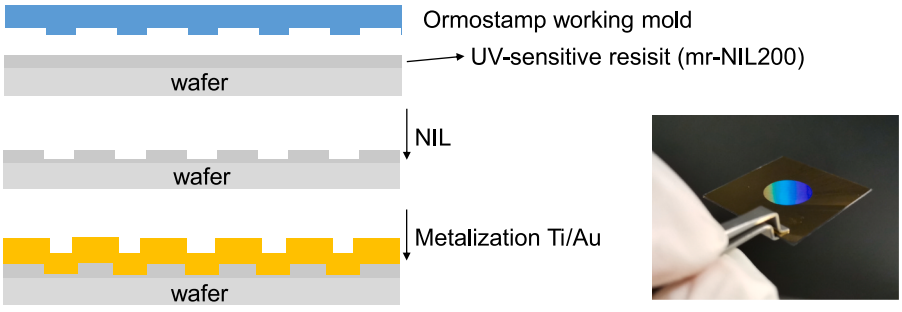

Fig. 1. Left: schematic view of the fabrication process, including the NIL process between the Ormostamp working mold and UV-sensitive resist, and the metallization process of 20 nm Ti and 40 nm Au layers. Right: a digital photograph of the AuNpA (diameter of the patterned area is 1 cm).

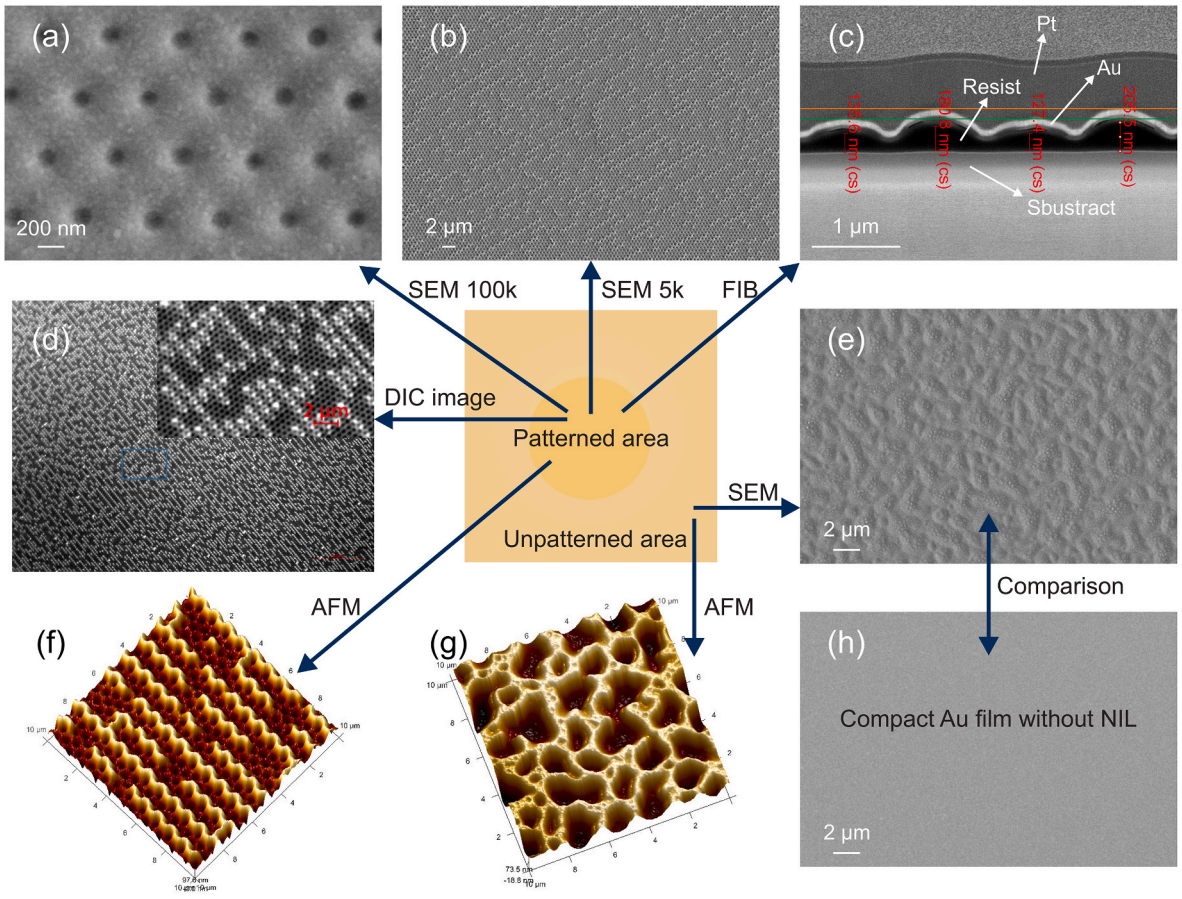

Fig. 2. SEM images of the fabricated AuNpA at 100 k magnification with scale bar of 200 nm (a) and at 5 k magnification with scale bar of 2 μm (b), FIB cross-section image (c) and DIC image (d) of the AuNpA with fringe structure, SEM image of unpatterned area after NIL (e), AFM image of the AuNpA on patterned area (f) and unpatterned area (g), SEM image of Au film without NIL for comparison (h). The central sketch of AuNpA is placed for illustrative purposes.

cally within a range of 5–20 nm leading to an enhanced quantum yield, reduced fluorescence lifetimes, and increased photo-stability. This phenomenon can be thought of as the metallic nanostructure functioning as an optical antenna, facilitating the conversion of propagating radiation into near-field energy. The quantum yield in free space (Q_0) can be quantified mathematically through the well-established formula [23,24]:

$$Q_0 = \frac{\Gamma_0}{\Gamma_0 + k_{nr}} \tag{2}$$

Equation (2) describes the quantum yield for an isolated fluorophore, where Γ_0 is the radiative rate and k_{nr} represents the non-radiative rate. In the presence of the optical antenna, the radiative rate is altered. The modified quantum yield (Q) can be expressed as [25]:

$$Q = \frac{\Gamma_0 + \Gamma_m}{\Gamma_0 + \Gamma_m + \Gamma_{nr} + k_{nr}} \tag{3}$$

From the above equations, a significant conclusion can be drawn: the additionally introduced radiation decay rate Γ_m competes with the non-radiation decay rate Γ_{nr}, thereby leading to either a fluorescence enhancement or a quenching. It is important to note that direct contact or very close proximity (less than 5 nm) to the metallic surface can lead to quenching of the fluorophores [23,24]. For our study, it is of importance that the maximum SPP peak was located at approximately 666 nm, while the MB fluorophore's excitation was at 668 nm, Fig. 3. The strong overlap observed between the SPP peak and the excitation peak of MB facilitates an enhancement of the excitation rate of the fluorophore compared to its value in free space. This enhancement arises due to Förster resonance energy transfer (FRET) at short distances between the

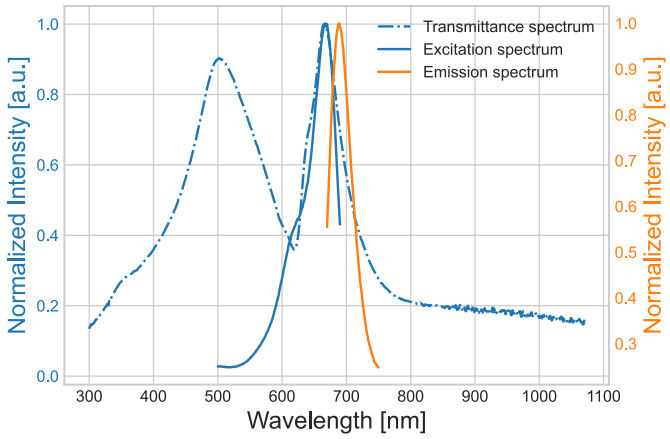

Fig. 3. SPP transmittance (dashed blue line) spectrum of AuNpA, excitation (blue line), and emission spectrum (yellow line) of 1 μM S1/S2_20T_MB in Tris buffer.

nanostructure and fluorophore (typically within approximately 15 nm), and the Purcell effect at more extended distances (in the range of 10–50 nm). The Purcell enhancement pertaining to plasmon radiation is usually of negligible significance, as the local density of optical states (LDOS) at substantial distances from the fluorophore is minimal. Owing to the trade-off between FRET and the Purcell effect, even slight variations in distance within the length of surface tethered aptamers (<15 nm) significantly influence excitation enhancement. Consequently, this

characteristic can be exploited for the construction of highly responsive sensors, which can detect minimal changes in the local environment of the electrode surface [24,26,27].

Hence, the precise determination of the optimal distance between the metallic surface and fluorophores is of critical importance. The concept underlying our aptasensor design is based on a two-strand oligonucleotide. The first strand S1 is 20 nucleotides long, designated to form a stem loop, and possesses a dithiol group with two thiol units to facilitate a strong binding to the gold surface. The second strand is complementary to S1, contains the C7 S protein aptamer and MB as fluorescence/redox probe. This strand is in total 39 nucleotides long, and is denoted as S2_MB. The third strand is identical to S2_MB but contains a thymine spacer. This ssDNA strand is in total 59 nucleotides long and denoted as S2_20T_MB. The inclusion of 20 thymine nucleotides serves as an extension to increase the distance between the gold surface and the fluorophore. The choice for thymine is based on the observation that nucleotide affinities for gold surface decline in the following order: A > G ≈ C ≫ T [28,29]. In our experimental design, the maximum surface distance of the label is constrained by the length of the double helix, which is approximately 20 nm for a 59-base pair construct if we don't take the DNA tilt into account. However, Lev et al. estimated the conformation of coiled single-stranded DNA and the average tilt of double-stranded DNA strands of varying lengths using spectral self-interference fluorescence microscopy. It was found that a 50-mer double-stranded DNA exhibits an estimated height of around 10.5 nm [30]. Therefore, in a simplified scenario of a rod hinged to the surface, where we employ relatively short stem-loop S1 strand as rigid rods attached to hinges, the average height of the distal label, assuming free rotation for half of its length, is characterized by an average tilt angle of 60° from the normal. Additionally, it should be noted that free rotation may be restricted due to steric constraints arising from nearby DNA molecules and interactions with the surface. As a result, we estimate the distance between the fluorophore and the gold surface for the long S1/S2_20T_MB configuration to be approximately 13 nm. It is essential to ensure such an adequate distance to prevent quenching effects. For comparison, a shorter S1/S2_MB conjugate without the additional 20 thymines is estimated to be around 9 nm in length.

To validate the hybridization of the two strands (S1 and S2_20T), NUPACK simulation and gel electrophoresis experiments were performed. The simulated secondary structure of the S1 + S2_20T complex possessed a calculated free energy of −26 kcal/mol, see Fig. S6a. Table S1 provides further insights into the simulation results, revealing that the complex formation of S1 + S2_20T has a yield of 99.9 %. This high percentage underscores the efficiency and stability of the hybridization process. For further confirmation of the hybridization, gel electrophoresis characterization was conducted, as illustrated in Fig. S6b. Lane 1 contains pure S1, while lane 2 holds S2_20T_MB. Significantly, in lane 3, a conspicuous presence of longer duplexes was observed when these components were mixed at room temperature for 2 h. This process separated the unhybridized S1 and S2_20T_MB fragments from their potentially hybridized form. After electrophoresis, we visualized and documented the gel using a Bio-Rad ChemiDoc Imaging System (Bio-Rad Laboratories GmbH, Feldkirchen, Germany). We observed a distinct band with lower migration mobility, which corresponded to the hybridized product of S1 and S2_20T_MB, thus confirming the success of the hybridization process.

The presence of plasmons also significantly influences the fluorescence lifetime, and in the context of a coupled system, the original lifetime τ_0 undergoes a change to τ, which is given by the following expressions [25]:

$$\tau_0 = \frac{1}{\Gamma_0 + k_{nr}} \tag{4}$$

$$\tau = \frac{1}{\Gamma_0 + \Gamma_m + \Gamma_{nr} + k_{nr}} \tag{5}$$

Therefore, FLIM measurements (with two-photon excitation at 925 nm) were employed to evaluate the kinetics of the excited-state decay as shown in Fig. S7.

To validate the PEF effect, we further conducted a series of direct fluorescence microscopy experiments, varying both the spatial locations and the choice of two distinct substrates. The obtained fluorescence microscopy images, accompanied by their corresponding intensity histograms, offer a comprehensive depiction of the optical characteristics of the respective sample. The analysis was applied to the specific areas of interest, which include the edge region between AuNpA and surrounding gold, the plasmonic AuNpA region, and only the plain Au film. The enhancement factor is determined according to Equation (6) [31,32]:

$$EF = \frac{I_{MB@AuNpA} - I_{AuNpA}}{I_{MB@Aufilm} - I_{Aufilm}} \tag{6}$$

where $I_{MB@AuNpA}$ is the fluorescence intensity of MB from the substrate of AuNpA, $I_{MB@Aufilm}$ is the fluorescence intensity from the referenced substrate of Au film, I_{AuNpA} and I_{Aufilm} are the background intensity of the pure AuNpA and Au film without fluorophore, respectively.

For the edge region, the AuNpA area and the surrounding gold can be clearly distinguished by low fluorescence intensities for the surrounding gold and high intensities with strong local variations for the nanopatterned area, all modified with the S1/S2_20T_MB, Fig. 4a. In the plot of the intensity distribution, three distinct peaks can be identified attributed to the unpatterened area, nanopits, and fringe area from left to right, each associated with varying levels of fluorescence intensity, Fig. 4b. This interpretation is confirmed by Fig. 4c and d, which show a similar surface with the same S1/S2_20T_MB modification but without the unpatterened area. In the intensity distribution plot, the low-intensity peak vanished while the high-intensity peaks persisted. Investigating the plasmonic fringe region after modification with the short DNA construct S1/S2_MB revealed a similar optical response but with lower overall intensity compared to the longer S1/S2_20T_MB hybrid, Fig. 4e and f. This observation suggests that the fluorophore of the longer dsDNA construct was located closer to the optimal MB-Au distance (PEF). Lastly, the fluorescence microscopy data obtained for the plane Au film modified with S1/S2_MB served as a reference, Fig. 4g and h. Here it becomes apparent that a distinct PEF effect was only observed within the plasmonic nanopit area. When compared to the Au film, the average enhancement factor for MB in the S1/S2_20T_MB hybrid was determined to be 5.33 and 7.60 for the AuNpA and the fringe structures, respectively, whereas, for the short S1/S2_MB configuration, the intensity was only 61.9 % compared to the S1/S2_20T_MB configuration.

In addition to the dual transduction probe MB, we also tested a combination of cyanine5.5 (Cy5.5) and ferrocene (Fc) as fluorescence and redox labels, which were attached to S2_20T and S1 terminals, respectively. The cyanine dyes as near-infrared (NIR) fluorophores (650–900 nm) are widely used as fluorescent probes for bioimaging because of their wide dynamic range, minimal background fluorescence, and high sensitivity [33]. The excitation (687 nm) and emission spectrum (708 nm) of S2_20T_Cy5.5 showed an enhancement factor of 53 to the Au film substrate, Fig. S8. This is distinctly higher than the enhancement observed for MB, however, we encountered a dramatic decrease in fluorescence intensity after 5 continuous electrochemical scanning. On the other hand, when we opted for MB as dual transduction label and conducted the potential cycling as depicted in Fig. S9, no electrochemical-induced quenching was observed. Apparently, the utilization of MB as dual transduction probe MB is better suited for our combined PEF-EC sensing approach, than a splitting of its function onto two separate probes one for PEF sensing (Cy5.5) and one for electrochemical detection (Fc). The intriguing phenomenon of electrochemical quenching, described here for the first time, deserves further in-depth investigation.

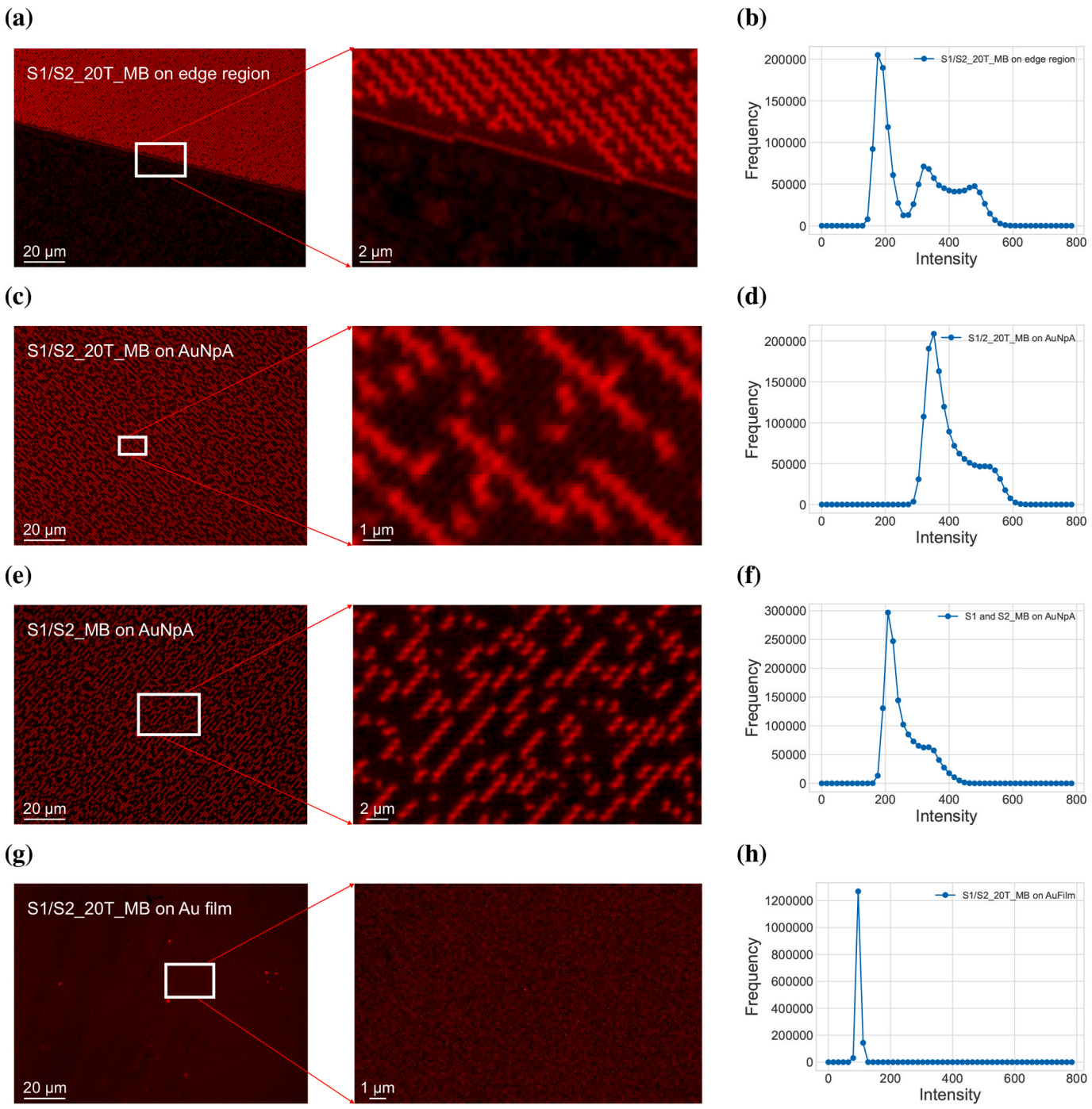

Fig. 4. Fluorescence microscopy images (all the images are adjusted using best fit to optimize display ranges) and intensity histogram of AuNpA edge region with long S1/S2_20T_MB (a, b), AuNpA plasmonic area with long S1/S2_20T_MB (c, d), AuNpA plasmonic area with short S1/S2_MB (e, f), Au film with long S1/S2_MB (g, h).

3.3. *FDTD simulation*

The transmittance spectra were modeled by FDTD simulations based on two distinct concepts reflecting the experimentally investigated samples: idealized fringe structures derived from geometric patterns and a more realistic framework based on AFM data obtained from a real sample containing the fringe structures, Fig. 5a. Although the experimental and simulated spectra did not display perfect congruence, the peak patterns exhibited a fundamental resemblance. Noteworthy, the AFM data included imaging artifacts in particular due to the superposition of sample topography and tip shape, which can be recognized when comparing FIB-SEM and AFM images, Fig. 2c and f. Nevertheless, the simulation derived from AFM data reflects the experimental transmission curve better than the idealized geometric model. The improved congruence can be attributed to the inclusion of fringe structures and the associated surface roughness, which collectively contribute to a more realistic representation of the experimental conditions.

The difference in enhancement factor between fringe and pit regions is associated with the amplification of the electric fields at those structural features. We further utilized FDTD simulation including the AFM data to investigate the cross-sectional distribution of the electric field, Fig. 5b and c. The electric field distribution in this model exhibited

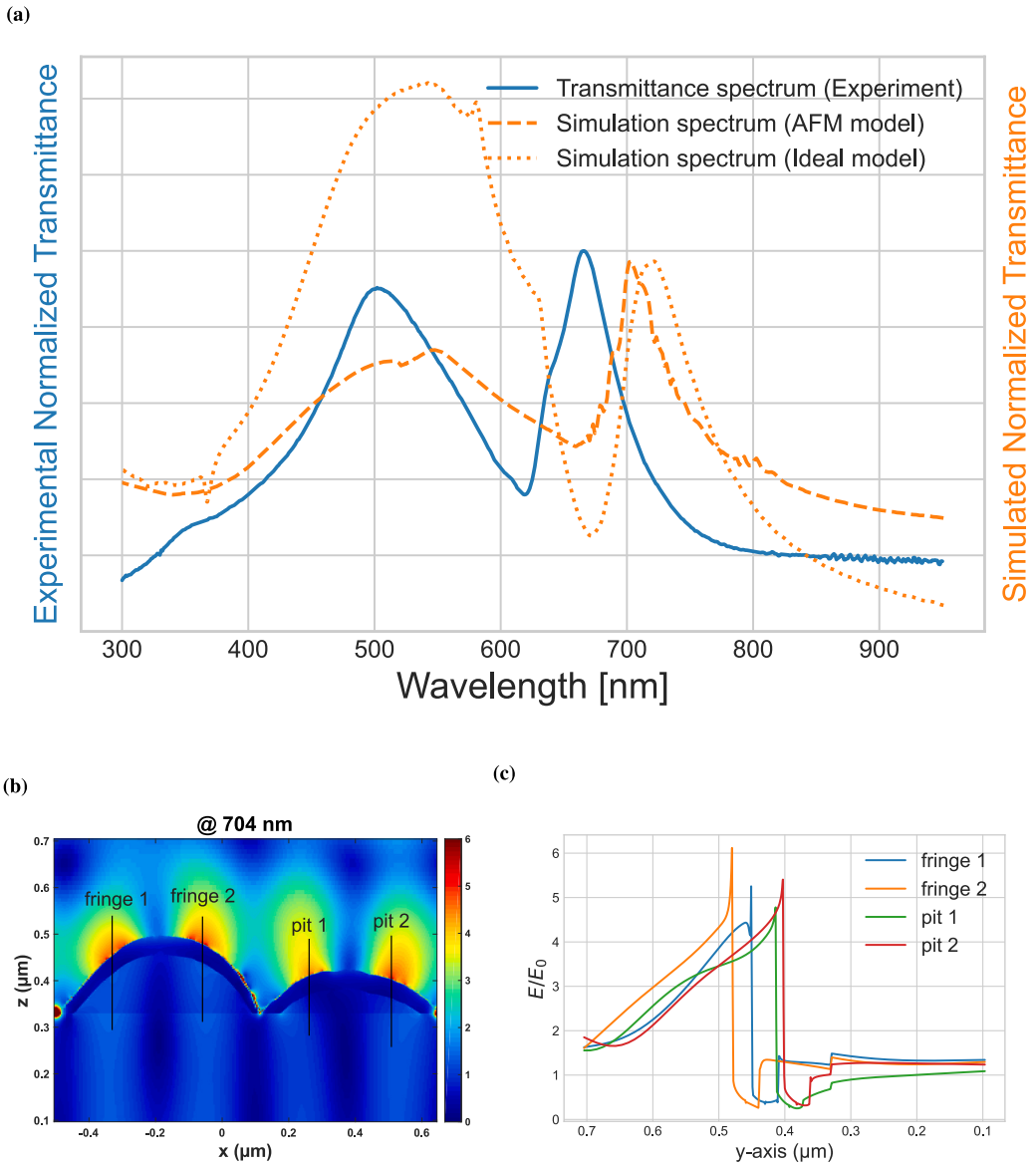

Fig. 5. Real transmittance spectrum of AuNpA and simulated transmittance from AFM and idea case (a), cross-sectional electric field distribution for AFM imported surface model (b), and z-component of the electric field with four decay channels (c).

distinct disparities between the elevated fringe structures and hole structures. Notably, the cross-sectional asymmetry resulted in four distinct electric field decay channels, labeled fringe 1, fringe 2, pit 1, and pit 2, Fig. 5b. For each decay channel, we analyzed the z-component of the electric field distribution (Fig. 5c) and identified the maximum electric enhancement (E/E_0) to be 5.3, 6.1, 4.6, and 5.4, with decay lengths of 177 nm, 176 nm, 252 nm, and 205 nm, respectively. The observed variations and asymmetry in both fringe and pit regions in the electric field enhancement and the decay length are noteworthy aspects of the PEF effect.

Regarding the fluorescence enhancement at the fringe structures, two hypotheses can be used to elucidate this phenomenon. Firstly, the prominent fringe structures may function as focusing elements due to the higher distance of the Au from the surface in comparison to the overall pit arrays [34,35]. Secondly, the discrepancy in decay length, as determined from FDTD simulations, could potentially result in varying optimal enhancement distances. It is hypothesized that S1/S2_20T MB may be located closer to the optimal optical enhancement distance within the fringe structures, contributing to the observed effects.

3.4. Aptasensor performance

For the implementation of the PEF-EC aptasensor, the assembly process and the associated stepwise immobilization of the molecules on the electrode surface were investigated using a QCM instrument equipped with a fluidic system. The observed frequency change was proportional to the increase in mass when molecules bind to the sensor surface, Fig. S10. This corroborates the occurrence of a dissociation process via the binding between the S2_20T_MB and the S protein, followed by detachment from the gold surface beside the stepwise immobilization of the receptor layer.

Before utilizing AuNpA, the immobilization process was additionally evaluated by surface plasmon resonance microscopy (SPR-M) employing a plane gold surface. As presented in Fig. S11, an increase in molecular layer thickness was observed after the addition of S1, 6-MCH, and S2_20T_MB representing the assembly of the receptor layer. The median value of the thickness of the molecular layer exhibited a noticeable decrease with the addition of 10 fg/mL of S protein (from 18.40 nm to 11.75 nm). A higher concentration of the S protein (1 pg/mL)

experienced a subsequent decrease (from 11.75 nm to 8.40 nm). These measurements corroborate the QCM data via a complementary surface plasmon-based technique. The entire procedure was recorded in video format, accessible as an attachment (SPR-M process.mp4).

Supplementary data related to this article can be found online at https://doi.org/10.1016/j.talanta.2024.126760

For the real sensor, we utilized the AuNpA as a substrate for both PEF and EC signal monitoring. Upon interaction with the S protein, the S2_20T_MB strand dissociated the hybridization with S1 and detached from the gold surface, Fig. 6a. Simultaneously, the surface tethered strand S1 is forcing into the formation of a stem-loop structure, which further supports the dissociation of the hybridization with S2_20T_MB. The release of the MB labeled S2-strand into the bulk medium leads to a drop of both sensor signals. These concentration-dependent alterations of the redox current and the enhanced fluorescence are exploited as dual sensor signals. The PEF transducer exhibited a distinct decrease in the fluorescence intensity, Fig. 6b–k. The corresponding DIC images are presented in Fig. S12. Plotting the overall fluorescence intensity of the image versus the concentration resulted in a calibration curve with a linear relation in a semi-logarithmic presentation, spanning a concentration range from 1 fg/mL to 10 ng/mL, Fig. 6l. The resulting calibration formula, $\Delta F/F_0 = 0.05$ lgC - 0.07, possessed a correlation coefficient of 0.98. Notably, the sensor achieved a limit of detection (LOD) of 0.07 fg/mL, determined according to the International Union of Pure and Applied Chemistry definition (IUPAC, 1997) as $X_L = X_B + 3X_B$, where X_B is the average value of blank measurement, and S_B is the standard

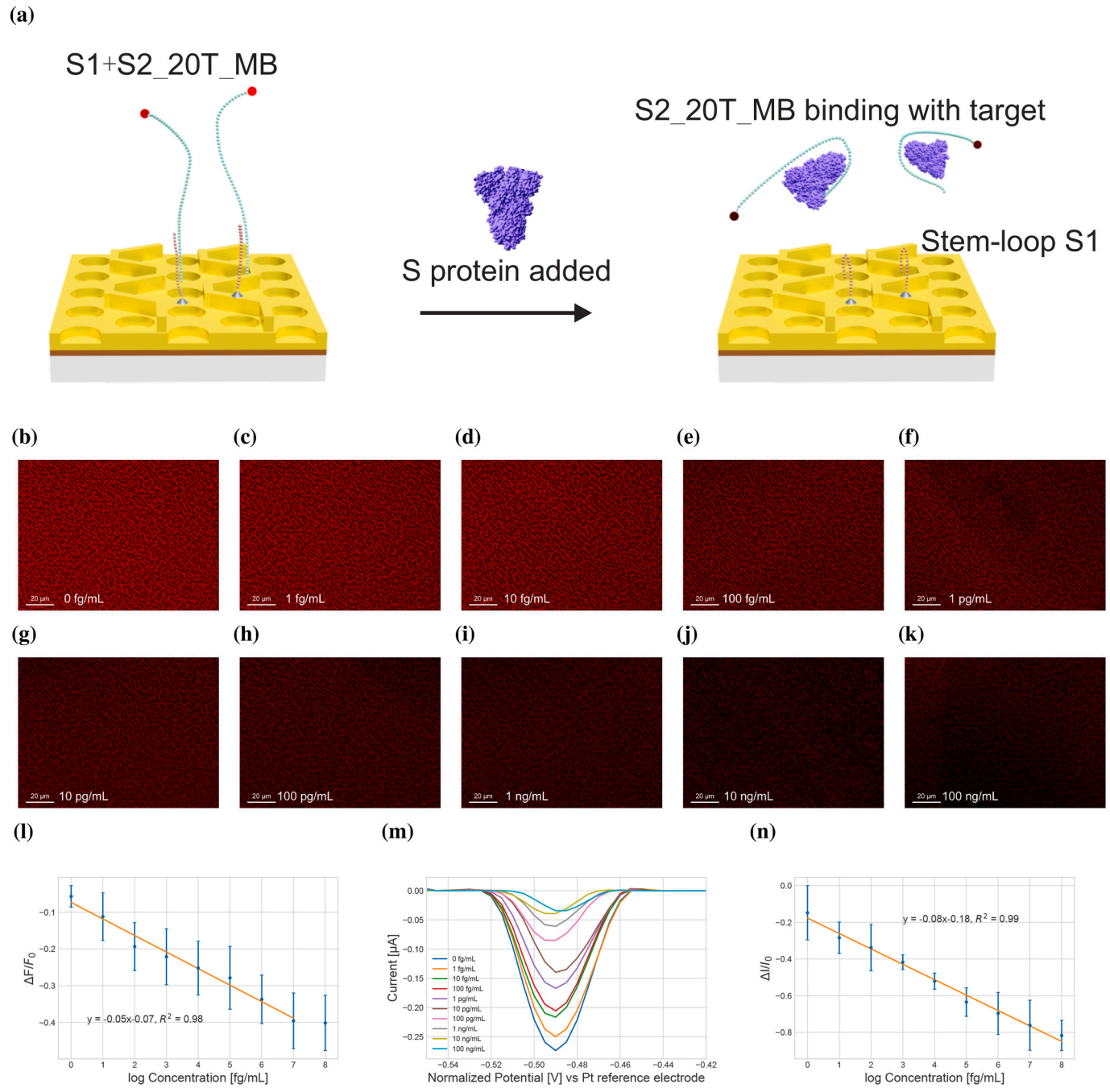

Fig. 6. Schematic illustration of the working principle for SARS-CoV-2 S protein detection based on AuNpA as substrate (a), fluorescence microscopy images of our aptasensor with different S protein concentrations from 0 to 100 ng/mL (b–k) and corresponding calibration curve (l), the normalized SWV current responses (m) and current change calibration curve (n) versus the logarithm of different S protein concentrations from 0 to 100 ng/mL.

deviation of the blank sample signal, and 3 is the numerical factor chosen according to the confidence level desired (95 %). The logarithmic relation of the concentration is based on the nature of the response curves observed in our experiments. The calibration curve practically represents an adsorption isotherm according to a Langmuir or a Langmuir-Freundlich model since the aptamer receptors are immobilized on the electrode and represent a defined number of adsorption sites on its surface. The occupation of these adsorption sites as a function of the analyte concentration gives the coverage, which is at first approximation proportional to the sensor signal [36,37]. To further evaluate the respective contribution influence of the fringe structure and the pit arrays on the sensor signal, an additional analysis was performed regarding the alterations in intensity values of the main peak (fringe structure) and minor peak (pit arrays) in relation to the S-protein concentration, Fig. S13. The resemblance in trends for both surface structures indicates that fringe structure and pit arrays contribute similarly to the overall PEF signal.

During the electrochemical detection, the SWV current response exhibited a decrease upon the addition of the S protein, Fig. 6m. Noteworthy, the peak position was corrected to a center position of −0.49 V to better recognize the drop in the peak height, since there was a stochastic potential shift of the redox peak. This was caused by the utilization of the Pt-wire pseudo reference electrode in this work, which was required to make it fit into the fluidic cell of this combined EC and fluorescence setup. The uncorrected SWV curves are displayed for comparison in Fig. S14. Also here, the $\Delta I/I_0$ response showed a semi-logarithmic dependence on S protein concentration, but with a wider concentration range spanning from 1 fg/mL to 100 ng/mL. The resulting calibration curve can be represented by the equation $\Delta I/I_0 = 0.08$ lgC - 0.18, with a correlation coefficient of 0.99, Fig. 6n. The corresponding detection threshold was 0.15 fg/mL. Thus, both transducers showed similar but not identical sensor characteristics, although both reported on the same binding event and even exploited the same MB-signal probe. The PEF sensor possessed a lower detection threshold, while the EC sensor was distinguished by a wider concentration range and higher sensitivity (slope of the calibration curve).

The selectivity for the aptasensors was analyzed by comparing the response to biomarkers of different viruses, which also befall the respiratory system, Fig. S15. Therefore, the aptasensor was exposed to solutions containing the Hemagglutinin/HA1 protein of the Influenza A H1N1, the response against glycoprotein G/RSV-G protein of the human respiratory syncytial virus (RSV), and the Spike protein of the middle eastern respiratory coronavirus (MERS). The used concentration for each biomarker of the respective viruses was 1 ng/mL. As a reference for comparison, we used the signals for the SARS-CoV-2 S protein also at 1 ng/mL, which were −33.71 % and −69.65 % for the PEF and EC transducer, respectively. The responses against the Influenza A biomarker were −0.56 % and 17.95 %, respectively, clearly lower than the responses for the actual analyte. Similarly, the response against the biomarker for the RSV virus was −8.72 % and 4.65 % again for PEF and EC transducer, respectively. Furthermore, against the MERS virus biomarker, the responses were −2.93 % and 21.92 %, respectively. All the PEF responses were considerably lower than the response to SARS-CoV-2 S protein. Noteworthy, the EC responses exhibited an inverse signal change resulting in increasing EC signals. This observation can be attributed to the non-specific association of these proteins to the aptamer, which may alter the S1/S2_20T_MB hybrid conformation. The unspecific binding did not induce dissociation of the protein-S2 complex but distorted the MB conformation and thus caused a shorter distance between redox probe and electrode resulting in enhanced redox currents. However, these interfering interactions and the associated current increases facilitate an easy and unambiguous differentiation between corresponding nonspecific, positive signal alterations and specific, negative signal changes due to S protein binding.

To further assess the practical performance and the robustness of the PEF-EC aptasensor in biological fluids, control experiments were conducted using a diluted 10 % human saliva matrix spiked with the S protein, employing the standard addition method (Table S2). The recovery values ranged from 102.3 % to 128.3 %, with relative standard deviation (RSD) values falling within the range of 2.0 %–17.7 % for PEF. For the EC transducer, the signal recovery was between 100.2 % and 110.7 %, with RSD values in a range between 2.5 % and 6.8 %. This suggests that the biosensor experienced minimal interference from human saliva, demonstrating a reliable robustness. The reproducibility was investigated by freshly preparing 3 samples modified with the same S1/S2_20T_MB. All electrodes exhibited a similar PEF and electrochemical response, and the RSD values were 8.43 % and 15.81 % respectively, demonstrating a satisfying reproducibility of the proposed biosensor. Furthermore, we tested the stability of the biosensor over 3 days. Fig. S16 shows the storage stability of the aptasensor after seating it in Tris buffer at 4 °C. After 3 days of storage, the PEF intensity didn't change much, and the current intensity stands around 75 % of its original intensity, which suggests the aptasensor is sufficiently stable for a single use detection, however, further optimization of the storing conditions need to be considered for long term storage. The characteristics of some previous studies for the quantitative analysis of S protein are presented in Table S3. The analytical parameters, including the detection limit and the linear range, are comparable to or better than in most other reports. Based on the recovery values obtained, we conclude that the assay performance of the PEF-EC aptasensor proves their potential for real diagnostic application.

In our previous study, we utilized a dual sensor where EOT and EC were combined [16]. In that sensor, the EC transducer showed a significantly lower LOD than the EOT transducer. In the present study, the optical PEF transducer exhibited a similar LOD as the EC transducer, suggesting that the utilization of the plasmons to enhance the fluorescence facilitates better sensor performances with lower LOD and wider concentration ranges than EOT transducers. The reason for this difference presumably is the surface confinement of the PEF, which is sensitive to minute changes of the fluorophore/substrate distance as a trade-off between FRET/quenching/Purcell effects with an optimal distance from the surface in the range of 10–15 nm [38]. Presumably, for the longer S1/S2_20T_MB conjugate, which is approximately 13 nm in length, the fluorophore is located at an optimal enhancement distance, while the shorter S1/S2_MB configuration (around 9 nm) without the additional 20 thymines, remains slightly below this optimal enhancement range. In contrast, the EOT sensor probes the entire attenuation length of the surface plasmon at the metal/liquid interface based on the overall refractive index change. As the refractive index of the DNA (n = 1.58 [39]) is similar to that of the proteins (e.g., bovine serum albumin with n = 1.60 [40]), the resultant signal generally may be less pronounced. Consequently, the EOT of periodic nanostructure arrays can be harnessed either by implementing easy to construct and operate but less sensitive sensor concepts, recording the peak shift of the transmitted light or by utilizing PEF, which facilitates low detection limits and wide detection ranges. In either case, the nanopit array facilitates complementary electrochemical and optical recordings to achieve reliable and redundant sensor signals.

4. Conclusions

This study reports on four main achievements: the fabrication of a large-scale AuNpA through an easy-to-perform nanoimprint lithography process, an enhancement of the PEF effect by fringe structures, the utilization of methylene blue as a dual-transduction label that facilitates the recording of fluorescence and electrochemical signals simultaneously, and the exploitation of this label for the development of a PEF-EC aptasensor for detecting the S proteins through simulations and experiments. The electric field distribution obtained from FDTD simulations and experimental transmittance spectra revealed a strong overlap between the SPP peak and the excitation peak of MB enabling a plasmon enhancement of the MB fluorescence by a factor of 5.33 on the AuNpA

and 7.60 for the fringe structures. Correspondingly, the enhancement from the fringe structure was higher than that of the underlying gold nanopit array. These AuNpA electrodes were used to develop an aptasensor for the specific detection of the SARS-CoV-2 S protein. The sensor showed similar detection characteristics with a detection threshold of 0.07 fg/mL and 0.15 fg/mL for PEF and EC transducer, respectively, covering the requirements for SARS-CoV-2 testing assays. Noteworthy, the plasmon facilitated fluorescence sensor was more sensitive than plasmonic sensors based on extraordinary transmission peak shifts. In summary, the findings of this work reveal a new strategy for the fabrication of plasmonic sensors based on arrays of nanostructures, the establishment of highly sensitive and redundant dual transducer sensors, the utilization of the same probe for fluorescence and electrochemical transduction, and an optimized competitive aptamer binding assay to advance current sensing technology of SARS-CoV-2 S protein detection which can be transferred to other sensor applications.

CRediT authorship contribution statement

Ruifeng Zhu: Writing – original draft, Visualization, Validation, Software, Methodology, Funding acquisition, Data curation, Conceptualization. **Mateo Alejandro Martínez-Roque:** Writing – review & editing, Methodology, Conceptualization. **Gabriela Figueroa-Miranda:** Writing – review & editing, Methodology, Conceptualization. **Ziheng Hu:** Writing – review & editing, Validation. **Adriano Acunzo:** Writing – review & editing, Software. **Hangyu Li:** Writing – review & editing, Data curation. **Qinyu Hu:** Writing – review & editing, Validation. **Justus Bednar:** Writing – review & editing, Data curation. **Thomas Gensch:** Writing – review & editing, Data curation. **Sven Ingebrandt:** Writing – review & editing, Supervision, Methodology. **Andreas Offenhäusser:** Writing – review & editing, Supervision, Methodology, Funding acquisition. **Dirk Mayer:** Writing – review & editing, Supervision, Methodology, Funding acquisition, Data curation, Conceptualization.

Declaration of competing interest

The authors declare that they have no known competing financial interests or personal relationships that could have appeared to influence the work reported in this paper.

Data availability

Data will be made available on request.

Acknowledgements

The authors thank Michael Prömpers for the fabrication of the master mold, Elke Brauweiler-Reuters for the FIB characterization, Ruben Stüttgen for the chamber fabrication by 3D printing, the Helmholtz Nano Facility (HNF) for the fabrication support, and Ruifeng Zhu gratefully acknowledges the financial support from the China Scholarship Council (No.201904910560).

Appendix A. Supplementary data

Supplementary data to this article can be found online at https://doi.org/10.1016/j.talanta.2024.126760.

References

[1] Hangping Yao, Yutong Song, Yong Chen, Nanping Wu, Jialu Xu, Chujie Sun, Jiaxing Zhang, Tianhao Weng, Zheyuan Zhang, Zhigang Wu, et al., Cell 183 (3) (2020) 730–738.
[2] Song Qi, Xindi Sun, Ziyi Dai, Yibo Gao, Xiuqing Gong, Bingpu Zhou, Jinbo Wu, Weijia Wen, Lab Chip 21 (9) (2021) 1634–1660.
[3] Deniz Sadighbayan, Ebrahim Ghafar-Zadeh, IEEE Sensor. J. 21 (9) (2021) 10219–10230.
[4] Yaofeng Zhou, Yuhao Wu, Lu Ding, Xiaolin Huang, Yonghua Xiong, TrAC, Trends Anal. Chem. 145 (2021) 116452.
[5] Pablo Alberto Franco-Urquijo, Mónica Sierra-Martínez, Mariana Jarquín-Martínez, Mateo Alejandro Martínez-Roque, Victor Miguel García- Velásquez, Gustavo Acosta-Altamirano, Nancy Jannet Ruiz-Pérez, Julia Dolores Toscano-Garibay, Luis marat alvarez-salas, Diagnostics 12 (11) (2022) 2829.
[6] Ziheng Hu, Yaqi Li, Gabriela Figueroa-Miranda, Simon Musal, Hangyu Li, Mateo Alejandro Martínez-Roque, Qinyu Hu, Lingyan Feng, Dirk Mayer, Andreas Offenhäusser, TrAC Trends in Analytical Chemistry, 2023 117021.
[7] Mateo Alejandro Martínez-Roque, Pablo Alberto Franco-Urquijo, Víctor Miguel García-Velásquez, Moujab Choukeife, Günther Mayer, Sergio Roberto Molina-Ramírez, Gabriela Figueroa-Miranda, Dirk Mayer, Luis M. Alvarez-Salas, Anal. Biochem. 645 (2022) 114633.
[8] Evair D. Nascimento, Wilson T. Fonseca, Tássia R de Oliveira, Camila Rstb de Correia, Vitor M. Faça, Beatriz P de Morais, Virginia C. Silvestrini, Henrique Pott-Junior, Felipe R. Teixeira, Ronaldo C. Faria, Sensor. Actuator. B Chem. 353 (2022) 131128.
[9] Mateusz Śmietana, Marcin Koba, Petr Sezemsky, Katarzyna Szot-Karpińska, Dariusz Burnat, Vitezslav Stranak, Joanna Niedziółka-Jönsson, Robert Bogdanowicz, Biosens. Bioelectron. 154 (2020) 112050.
[10] Abbas Abid Suhad, Ahmed Muneer Ahmed, Israa MS. Al-Kadmy, Anas A. Sattar, Amany Magdy Beshbishy, Gaber El-Saber Batiha, Helal F. Hetta, Life Sci. 273 (2021) 119117.
[11] Tianyi Chen, Jialin Xin, Shwu Jen Chang, Ching-Jung Chen, Jen-Tsai Liu, Adv. Mater. Interfac. 10 (8) (2023) 2202202.
[12] Diming Zhang, Yanli Lu, Jing Jiang, Qian Zhang, Yao Yao, Ping Wang, Bilian Chen, Qiaoyuan Cheng, Gang Logan Liu, Qingjun Liu, Biosens. Bioelectron. 67 (2015) 237–242.
[13] Maxime Couture, Ludovic S. Live, Anuj Dhawan, Jean-francois masson, Analyst 137 (18) (2012) 4162–4170.
[14] Shaopeng Wang, Xinping Huang, Xiaonan Shan, Kyle J. Foley, Nongjian Tao, Analytical chemistry 82 (3) (2010) 935–941.
[15] Bohdan Lenyk, Gabriela Figueroa-Miranda, Ivan Pavlushko, Young Lo, Julian A. Tanner, Andreas Offenhäusser, Dirk Mayer, Chemelectrochem 7 (22) (2020) 4594–4600.
[16] Ruifeng Zhu, Gabriela Figueroa-Miranda, Lei Zhou, Ziheng Hu, Bohdan Lenyk, Sven Ingebrandt, Andreas Offenhäusser, Dirk Mayer, Nanomaterials 13 (16) (2023) 2374.
[17] Ting Guo, Changtong Wu, Andreas Offenhäusser, Dirk Mayer, physica status solidi (a) 217 (13) (2020) 1900924.
[18] Tomasz Cwalinski, Wojciech Polom, Luigi Marano, Giandomenico Roviello, Alberto D'Angelo, Natalia Cwalina, Marcin Matuszewski, Franco Roviello, Janusz Jaskiewicz, Karol Polom, J. Clin. Med. 9 (11) (2020) 3538.
[19] Jiafu Chang, Wenxin Lv, Qian Li, Haiyin Li, Feng Li, Anal. Chem. 92 (13) (2020) 8959–8964.
[20] By Kasem K Kasem and Stephanie Jones, Platin. Met. Rev. 52 (2) (2008) 100–106.
[21] Rajib Biswas and Nirmal Mazumder. Springer Nature, 2022.
[22] William O.F. Carvalho, J ricardo mejía-salazar, Sensors 20 (9) (2020) 2488.
[23] Seungah Lee, Seong Ho Kang, Biosensors 13 (3) (2023) 376.
[24] Ming Li, Scott K. Cushing, Nianqiang Wu, Analyst 140 (2) (2015) 386–406.
[25] Sarah Madeline Fothergill, Caoimhe Joyce, Fang Xie, Nanoscale 10 (45) (2018) 20914–20929.
[26] Siqi Gao, Renbin Zhou, Soham Samanta, Junle Qu, Tymish Y. Ohulchanskyy, Anal. Chim. Acta 1254 (2023) 341086.
[27] Mohsin Ali Badshah, Na Yoon Koh, Abdul Wasy Zia, Naseem Abbas, Zahra Zahra, Muhammad Wajid Saleem, Nanomaterials 10 (9) (2020) 1749.
[28] Hao Pei, Li Fan, Ying Wan, Min Wei, Huajie Liu, Yan Su, Nan Chen, Qing Huang, Chunhai Fan, J. Am. Chem. Soc. 134 (29) (2012) 11876–11879.
[29] Sarah M. Schreiner, David F. Shudy, Anna L. Hatch, Aric Opdahl, Lloyd J. Whitman, Dmitri Y. Petrovykh, Analytical chemistry 82 (7) (2010) 2803–2810.
[30] Lev Moiseev, M. Selim Ünlü, Anna K. Swan, Bennett B. Goldberg, Charles R. Cantor, Proc. Natl. Acad. Sci. USA 103 (8) (2006) 2623–2628.
[31] Zhenglong Zhang, Yanni Wu, Jun Dong, Wei Gao, Qingyan Han, Hairong Zheng, J. Phys. Condens. Matter 28 (36) (2016) 364004.
[32] Faheng Zang, Zhijuan Su, Liangcheng Zhou, Krishnamurthy Konduru, Gerardo Kaplan, Stephen Y. Chou, Adv. Mater. 31 (30) (2019) 1902331.
[33] Cheng Ying, Na Wang, Zhenxing Ren, Chenggang Xu, J. Microbiol. Methods 197 (2022) 106479.
[34] Antonio Minopoli, Adriano Acunzo, Bartolomeo Della Ventura, Raffaele Velotta, Adv. Mater. Interfac. 9 (2) (2022) 2101133.
[35] Brendan Dyett, Qiming Zhang, Qiwei Xu, Xihua Wang, Xuehua Zhang, ACS Cent. Sci. 4 (11) (2018) 1511–1519.
[36] Gabriela Figueroa-Miranda, Yuanying Liang, Mohit Suranglikar, Matthias Stadler, Nagesh Samane, Marcel Tintelott, Young Lo, Julian A. Tanner, Xuan T. Vu, Joachim Knoch, et al., Biosens. Bioelectron. 208 (2022) 114219.
[37] Andrea Idili, Claudio Parolo, Gabriel Ortega, Kevin W. Plaxco, ACS Sens. 4 (12) (2019) 3227–3233.
[38] Antonio Minopoli, Bartolomeo Della Ventura, Bohdan Lenyk, Francesco Gentile, Julian A. Tanner, Andreas Offenhäusser, Dirk Mayer, Raffaele Velotta, Nat. Commun. 11 (1) (2020) 6134.
[39] Takashi Inagaki, R.N. Hamm, ET arakawa, and LR painter, The journal of chemical physics 61 (10) (1974) 4246–4250.
[40] Yoh Sano, J. Colloid Interface Sci. 124 (2) (1988) 403–406.